Peer reviewed version

University of Bristol - Explore Bristol Research
General rights

NUMERICAL INVESTIGATION OF INITIAL CONDITION EFFECTS ON RAYLEIGH TAYLOR INSTABILITY WITH ACCELERATION REVERSALS

Denis Aslangil*, Arindam Banerjee[1]

*Department of Mechanical Engineering & Mechanics,
Lehigh University, Bethlehem, PA 18020 USA

Andrew Lawrie^

^ Department of Mechanical Engineering, University of Bristol,
Queen's Building, University Walk, Clifton BS8 1TR UK

---

[1] Corresponding author: Associate Professor, Department of Mechanical Engineering and Mechanics, Lehigh University, Bethlehem, PA 18020, USA. Email: arb612@lehigh.edu Phone: 1-610-758-4099

ABSTRACT

The influence of initial conditions on miscible incompressible baroclinically driven Rayleigh-Taylor instability undergoing non-uniform acceleration is explored computationally using an Implicit Large Eddy Simulation (ILES) technique. We consider the particular case of evolution during multiple reversals of acceleration direction, where the flow is alternately statically stable or unstable. In the unstable phase, the flow is driven by the baroclinic release of potential energy, whereas in the stable phase, work is done against the density stratification with the energy exchange taking place by wave-like mechanisms. These dynamics are fundamentally different; here, we track the evolution of volume-averaged turbulent statistics that are most sensitive to changes in the distribution of spectral power and bandwidth of the initial conditions as the flow alternates between dynamical regimes due to acceleration reversal.

1. INTRODUCTION

Rayleigh-Taylor Instability (RTI) [1, 2] occurs at a perturbed planar interface between a light fluid (ρ_L) and a heavy fluid (ρ_H) in the presence of an acceleration field in a direction normal to the interfacial plane. Traditionally, the study of RTI has focused on acceleration fields that are constant and includes various natural and industrial flows such as combustion and chemical reactor processes [3, 4] pollutant dispersion [5], certain geological processes and oceanic current flows [6, 7]. However, there exist several applications in which RTI appears in non-uniform acceleration fields; these include blast waves, inertial confinement fusion [8, 9] and the stellar dynamics of Type Ia supernovae [10, 11]. Variations in acceleration are known to alter the dynamics of the RTI induced mixing process, and our primary motivation is to investigate the effects of initial conditions (ICs) on the late-time evolution of the instability towards turbulence under acceleration reversal. We characterize small but finite perturbations to the interface as having height, h_0, and wavelength, $\lambda = 2\pi/k$. For sufficiently small initial perturbations relative to the perturbation wavelength, (i.e. $h \ll 1/k$), the interface perturbations grow exponentially according to [12]

$$h(t) = h_0 \cosh(\Gamma t), \tag{1}$$

where, $\Gamma = \sqrt{A_t g k}$ is defined as the classical RTI growth rate; and, A_t, the Atwood Number, is the non-dimensional density difference between the two fluids and is defined as $A_t = (\rho_H - \rho_L)/(\rho_H + \rho_L)$, which can range between values of 0 and 1 [13]. At late times (which we take as $h > 1/k$), the growth of individual modes saturates to a terminal velocity, but the

3

evolution of a broad spectrum of initial spatial wavelengths follows a parabolic envelope [14]. This semi-empirical observation can be confirmed using dimensional analysis as [15, 16]

$$h_{b,s} = \alpha_{b,s} A_t g t^2,$$ (2)

where, h_b is the bubble height (penetration of light fluid into the heavier one), and h_s is the spike height (heavy fluid penetration into the lighter one with subscript b indicating bubbles and s indicating spikes); g is the acceleration; t is the time; and $\alpha_{b,s}$ is the growth rate parameter. For miscible fluids, a region of fluid with density intermediate between ρ_L and ρ_H emerges. This region is symmetric about the location of the initial interface at low A_t numbers, and rising (buoyant) structures, known as bubbles, grow at a similar rate to falling (relatively dense) structures, known as spikes; the respective growth rate coefficients are equal $\alpha_b \approx \alpha_s$. As the density difference between the two fluids increases, this symmetry breaks down as the spikes penetrate into unmixed regions of ρ_L faster than bubbles penetrating into ρ_H; this results in α_s > α_b with $\alpha_s \rightarrow$ ½ as $A_t \rightarrow 1$. In this study, we have chosen a moderate A_t number ($A_t = 0.5$), in order to investigate the influence of asymmetric growth undergoing acceleration of alternating direction. Eq. (2) shows that the mixing width grows quadratically with time and reaches a self-similar length scale ($A_t g t^2$) at late times where the flow is deemed to have lost memory of its ICs [12]. However, there a universal value for the growth parameters α_b and α_s is not known and systematic discrepancies in measured values between experimental and numerical studies are attributed to the choice or selection of ICs, [12, 17-19]. Computational studies on RTI with constant acceleration by Ramabraphu et al. [19] and Banerjee and Andrews [12] have investigated the effect of spectral bandwidth, spectral shape, and discrete banded spectra; for

4

verification and comparison, we have chosen our ICs to match closely those used in these earlier studies.

Compared with the literature on RTI with constant acceleration, the variable acceleration problem (including cases with acceleration reversal) has received relatively little attention. To date, there is only one experiment (that uses immiscible fluids) [20] and a limited number of simulation efforts [13, 21, 22] that have explored this problem. There is currently very weak understanding of how ICs affect the late-time evolution of a time varying RTI, and this novel aspect is the focus of the present work. We explore the role of ICs on RTI undergoing multiple acceleration reversals and compare it to the classical RTI with constant acceleration. In our problem, the acceleration is reversed multiple times; the flow starts with an initially destabilizing acceleration (Accel phase, $g>0$) followed by the first reversal to a stabilizing acceleration (Deccel phase $g<0$). A second reversal reverts the instability back to the Accel phase ($g>0$). Such a time varying RTI problem has been called the Accel-Deccel-Accel (ADA) problem [22, 23]. The non-dimensional time $\tau = A_t \sqrt{gt^2/L}$ selected for the first acceleration reversal is chosen to ensure that the simulated flow is tending towards self-similarity before reversal. Small statistical inhomogeneities in the spatial distribution of wave modes perturbing an interfacial plane of finite extent in the computational domain can lead to early nonlinear mode coupling that is non-self-similar for a short period; the objective is to position our acceleration reversals long after such early transients have occurred.

RTI with variable acceleration histories has been investigated using the Linear Electric Motor (LEM) experiment [20, 23]; however, the experiments used immiscible fluids at maximum Atwood numbers of 0.48 [23]. In their 1996 experimental study, Dimonte and Schneider [20] investigated four different acceleration histories that included a constant,

5

increasing, decreasing, and impulsive accelerations generated using the LEM. They reported that increasing acceleration ($\dot{g} > 0$) leads to faster growth of h_b than constant and in decreasing acceleration ($\dot{g} < 0$) histories. A subsequent publication by Dimonte et al. [23] used the gradual ADA profile (not a step function) in which they observed shredding of identifiable structures in the flow, i.e. decomposition of the modes of dominant bubbles and spikes during the deceleration phase. Shredding appears to produce a temporary increase in molecular mixing that then delays re-initiation of mixing layer growth upon the second reacceleration. Recently, Ramaprabhu et al. [22] simulated RTI using a similar ADA profile to the Dimonte experiment [23] for both a single wavenumber (A_t=0.15 and 0.9), as well as a spectrum of wavenumbers with (A_t=0.5). The results were obtained using a massively parallel Implicit Large Eddy Simulation (ILES) code, MOBILE, and were in good agreement with experimental results. The study concluded that swapping acceleration rapidly changes the structure of the flow. Since the acceleration phase in RTI is marked by substantial anisotropy in the mixing region; decelerating the system induces a rapid increase in the rate of molecular mixing and decreases anisotropy within the mixing region. Upon re-acceleration, anisotropic self-similar RT is resumed, albeit from an 'initial' state perturbed with both scalar spectral power and substantial kinetic energy. Livescu et al. [13] and Livescu and Wei [21] ran direct numerical simulations (DNS) of RTI with acceleration reversal and similarly reported that after acceleration reversal the molecular mixing increases within the flow. Their preliminary results also showed that the large-scale anisotropy decreases within the inner region of the mixing layer; although, interestingly, at the edge regions of the mixing layer, increases in small-scale anisotropy can be attributed to local buoyancy forces. The observation that anisotropy is non-uniform throughout the mixing region motivates us to consider that ICs

may continue to play an important role in the flow evolution even during deceleration and re-acceleration periods.

In our present work, four different ICs were carefully imposed on the RT problem under variable acceleration histories to investigate the effects of: (a) spectral bandwidth and (b) spectral power distribution on the subsequent evolution of RTI. We choose the benchmark ADA acceleration history similar to the one used by Ramaprabhu et al. [22] to eliminate any variability that may result due to choice of more physical acceleration histories similar to blast waves or ICF implosions. Our objective is to investigate the mechanisms that are common to the first acceleration and the re-acceleration period, unravel the sensitivity of long-term flow evolution to acceleration reversals and the effect of ICs on these processes. In this study, we present a range of volume-averaged and horizontally averaged metrics, the mean concentration, the mixing layer growth rate, the molecular mixing parameter, second order moments. The anisotropy tensors and second order moments are presented with their spatial profiles since we view this information as particularly instructive. The remainder of this paper is organized as follows: in § 2 the numerical method and problem setup are described. The results of the self-similar analysis and effects of ICs for two different acceleration histories are reported in § 3. Finally, we summarize our findings in § 4.

2. NUMERICAL METHOD AND PROBLEM SET

2.1. MOBILE

MOBILE is a Navier-Stokes solver for three-dimensional, variable-density volume-conserving flows, using a finite volume approach [24-26]. Mass and momentum equations are solved using a fractional step approach, separating hyperbolic (advective transport), parabolic

(scalar diffusion and viscous dissipation) and elliptic (pressure and velocity correction) contributions and using efficient, specialized second/third order numerical methods for each part. The advection algorithm is strictly monotonic, with a van-Leer approach to gradient limiting and uses a compact stencil that converges between 2nd and 3rd order. The parabolic operations are chosen to be semi-implicit or explicit as required for computational efficiency. After source terms, parabolic and hyperbolic elements are accounted, the velocity field is no longer volume-conserving and requires correction. The projection of this intermediate velocity field onto the nearest vector field in the space of divergence-free fields follows the well-known Hodge-Helmholtz decomposition [27], and exactly conserves discrete angular momentum (a quantity of considerable interest in baroclinic flows), though by construction local conservation of linear momentum cannot be satisfied through the projection. The pressure Poisson equation intrinsic to this projection technique is solved by an efficient parallel multigrid algorithm. A parallel macro language interpreter supports convenient on-the-fly computation of turbulent statistics for post-processing and visualization.

Scalar, density and the three momentum components are split into sequences of *x-y-z-z-y-x* one-dimensional update instructions, following Strang [28] to improve temporal orders of convergence without appreciable performance penalty. These one-dimensional advection sub-problems are solved with methods that are consistent with the fundamental physical principle of total variation boundedness (TVB), a simple strategy guaranteeing the absence of spurious oscillations at the end of the full three-dimensional update. To satisfy this requirement while also retaining a higher order of accuracy in most regions of the flow, we follow the MUSCL approach. The left and right states of the single-wave Riemann problem are modified by using piecewise polynomial reconstruction, and Godunov's exact solution with these modified states is

used to specify fluxes across cell faces. In regions of the flow with a sufficiently slow variation of scalar, density and momentum a linear polynomial is used (and in isolation would produce a scheme of globally second order convergence). In regions surrounding steep gradients aligned with the direction of the advection sub-problem, the reconstruction is chosen to interpolate between a low order (constant) and higher order (linear) polynomial to supply just sufficient additional numerical viscosity to satisfy the TVB condition.

The staggered grid approach is used, which suppresses mesh-scale numerical oscillation without the need to add artificial viscosity and requires only one elliptic solve per iteration. Scalar finite volumes have velocities supplied at all faces; momentum is computed in offset finite volumes with interpolated values. The current work uses Implicit Large Eddy Simulation (ILES), a method in which energy dissipation that concentrates at small scale around steep gradients of velocity is accounted for by locally increased numerical viscosity that is required to satisfy the TVB principle. While physical dissipation is conveniently spatially coincident with regions requiring additional numerical viscosity, there is one important distinction: physical viscosity in a Newtonian fluid is inherently isotropic, whereas the required numerical viscosity is not necessarily. In strongly turbulent flows where small-scale vortical flow features are approximately circular, such directional distinctions often happen to be averaged out. However, this is not the case in general. In MOBILE therefore, care is taken to ensure that interpolation between polynomial reconstructions is computed isotropically. While there is a small penalty on the preservation of spatial gradients per unit of computational cost, simulations performed in this manner offer a complete representation of the viscous stress tensor without incurring the severe restriction on Reynolds number per unit of the computational cost that a careful Direct Numerical Simulation (DNS) imposes. MOBILE, used in ILES mode, produces dissipative

spectra in RTI consistent with the expected $E(k) \sim k^{-3}$ scaling, which is comparable with observed values in experiments [29, 30] and DNS calculations made by other codes [31, 32]. However, ILES cannot be grid independent: the minimum represented length-scale is set by the grid spacing directly and not (as in the case of conventional modelled-dissipation LES) by parameters that are functions of the grid-scale.

2.2.　　Problem Setup

In the current work, as seen in Fig. 1, the computational domain has dimensions $L{\times}L{\times}3L$ (1 cm $\times$ 1cm $\times$ 3cm) with acceleration in the long, z, direction. Applied acceleration [0, 0, g_z (t)], is normal to a density interface at $z = 0$. Zero-flux conditions are imposed in the z-direction, periodicity in the x- and y-. An Atwood number of 0.5 was selected to compare with a range of existing literature. The ICs were created as out-of-plane perturbations h_0 (x,y) and then converted to volume fractions as follows [12]:

$$f_1(x, y) = \begin{cases} 1 + h_0(x, y)/\Delta, & for \quad h_0 < 0 \\ h_0(x, y)/\Delta, & for \quad h_0 > 0 \end{cases} \tag{3}$$

where, Δ is the width of the (cubic) computational cell. In the simulations reported here, the resolution was 256$\times$256$\times$768 (approximately 8 GB of RAM), spread over twelve cores of an HPz820 workstation with a turnaround time of 1-2 weeks per simulation. Validation and convergence of MOBILE on RTI problems have already been reported in Ramaprabhu et al. [22]. In the subsequent sections, capital letters are used for whole values, angle　brackets　are used for means and lower-case letters are used for fluctuations such as the decomposed value of the instantaneous velocity is: V= <v>+v.

2.2.1. Initial Conditions (ICs)

ICs were selected to quantify the influence of spectral index and spectral bandwidth (see Fig. 2). That all simulations have the same initial energy is a crucial property for objectively comparing ICs profiles. The perturbation function (Eq.4) [17] is used to supply h_0 (x,y):

$$h_0 = \sum_{kxky} a_k \cos k_x x \cos k_y y + b_k \cos k_x x \sin k_y y +$$

$$c_k \sin k_x x \cos k_y y + d_k \sin k_x x \sin k_y y \tag{4}$$

where $k = \sqrt{k_x^2 + k_y^2}$ and a_k, b_k c_k and d_k are Fourier amplitude coefficients. These coefficients are initially created to be distributed uniformly and pseudo-random within an annulus of the Fourier plane and zero elsewhere. A spectral index is applied to bias energy towards one end of the wavenumbers spectrum. When re-normalized, this distribution gives the same *r.m.s.* amplitude of ~ 3.15×10^{-4} L for all simulations and the energy density spectrum is calculated as:

$$\frac{\overline{h_0'^2}}{2} = \int_{k_{min}}^{k_{max}} E_{h0}(k) dk \tag{5}$$

We first consider an IC, denoted AS(0) in subsequent discussion, with mode numbers restricted to the narrow band of ($n = k / 2\pi$) 32-64. The spectral index (SI) is set to 0 as a benchmark for comparison with the constant gravity α-group study [17] [see Table 1: Case AS(0)-CG] to the time- varying ADA profile [Case AS(0)]. To test the effect of ICs, we chose two additional cases. The first one is a narrow band ICs with SI = -2, that indicates a higher proportion of initial energy in large wavelengths [Case AS(-2)]. The second one is a broadband IC with energy in modes 4-64 with SI=0 [Case BB]; broadband ICs has been demonstrated to represent better the initial energy distribution reported in RTI experiments[12, 19].

11

2.2.2. Acceleration Histories

Variable acceleration histories are important in understanding certain classes of complex mixing problems [23] and have been previously studied by numerous researchers [13, 22, 23, 33-35]. In the current work, we evolve the four different ICs in Table 1 according to a time varying ADA history. The results are compared with constant gravity computations which use directly comparable ICs. The ADA profile is chosen to represent the acceleration profile of the LEM experiments [23]. Ramaprabhu et al. [22] used the LEM acceleration profile and varied the acceleration values (g_0: 2cm/s^2, 4cm/s^2 and 8cm/s^2)to influence the non-linear development stage of the flow at which acceleration reversal occurred . We chose the case $g_0 = 4$cm/s^2 for benchmarking our simulations and subsequently focus our attention on the effects of ICs under ADA time-histories. The acceleration profile we use is approximated by the Heaviside (step) function as:

$$g_z = g_0 \{1 - H(t-2)(2) + H(t-4)(2)\} \tag{6}$$

The Heaviside function represents the time t_{swap} at which acceleration swaps direction and is represented as:

$$H(t - t_{swap}) = \begin{cases} 0 :: t < t_{swap} \\ 1 :: t > t_{swap} \end{cases} \tag{6a}$$

The system switches from an RT-unstable mixing problem extracting potential energy from a statically-unstable density stratification to a wave-like regime where kinetic energy does work against a mean stable stratification. Classic RTI returns upon re-acceleration though this time the ICs is highly perturbed with large perturbations, continuous mean density gradients and significant initial kinetic energy. All simulations were terminated when the bubble height reached *0.45x3L* to prevent distortion of the horizontally averaged statistics by the velocity

12

potential response of zero-flux top and bottom boundaries. Following [22, 23, 36], we introduce parameter U and Z to generalize Eq. (2) to variable acceleration:

$$U(t) = \int_0^t g(t')dt', \tag{7}$$

By integrating velocity once, we obtain the related length-scale interface displacement $Z(t)$ as [22]:

$$Z(t) = \int_0^t U(t'')dt'' = \int_0^t \int_0^{t''} g(t')dt'dt'', \tag{8}$$

where t' and t'' are integrands and arbitrary. It is well-known that bubble and spike heights and $Z(t)$ vary quadratically with respect to time [22, 36]; hence we would expect $h_{b,s}$ to grow linearly $h_{b,s} = 2\alpha_{b,s}A_tZ(t)$ for constant acceleration histories. Acceleration, velocity, and length scale Z (t) profiles versus time can be seen for our data in Fig.3.

3. RESULTS

In this section, we explore how ICs influence the evolution of RTI in the non-self-similar case of variable acceleration. We report the evolution of a range of parameters under ADA acceleration history, which includes the RT growth-rate ($\alpha_{b,s}$), the atomic mix parameter (θ) as well as second order moments, scalar variance, mass flux and vertical velocity variance. These measurements provide an essential distillation that is required to validate modelling assumptions, and in this multi-regime problem we provide a resource that can address several more general classes of interwoven energetic, horizontally homogenous stably and unstably stratified mixing, as is known to occur frequently in oceanic mixing near critical Richardson numbers [37].

13

The influence of ICs on classical RT-unstable flows has received considerable attention in the literature [12, 19, 38-41]. Previous studies [17, 42] have identified two alternative phenomenological models that describe the convergence towards self-similarity (Eq. 2) in the classical case of RTI with a broad-band multimode initial perturbation undergoing constant acceleration. The first such approach, known as *bubble merger*, considers that two or more bubbles may merge and form larger structures as a part of a continuous and repetitive process during the evolution of the mixing layer [17, 19]. In contrast, *bubble competition* involves amplification and saturation of long wavelengths and they lead the flow. Haan [43] postulated that the transition to nonlinearity is triggered when the sum of modal amplitudes reaches ~σ/k, implying that individual modes may become non-linear well before their amplitudes reach the non-linear threshold (σ) due to the interaction of adjacent modes. Several studies on constant acceleration RTI [12, 18, 19, 44] have shown that it is possible to control the time elapsed before structures in the flow develop full non-linearity, by modifying the initial amplitudes of modes so some saturate more quickly than others. Mean growth rates of the mixing layer become correspondingly modified. Several of these studies employed the RTI-3D code [12, 19, 23, 45] and demonstrated that ICs with longer wavelengths lead to a faster growth of the mixing layer width, producing values of the growth coefficient ($\alpha_{b,s}$) similar to that reported in experiments [29, 46]. Here we follow the definition of Ristorcelli and Clark [47] in calculating a time-dependent growth rate for the mixed layer thickness ($\alpha_{b,s}$):

$$\alpha_{b,s} = \frac{\dot{h}_{b,s}^2}{4A_t g \ h_{b,s}} \tag{9}$$

and their self-similar analysis for early time concluded with a quadratic form of the mix-width:

$$h(t;,C_0,h_0) = \frac{1}{4}AgC_0t^2 + \sqrt{AgC_0h_0}\,t + h_0 \tag{10}$$

14

which determines the early time evolution of half width of the mixing layer (for low A numbers, $h_b \sim h_s \sim h$). In Eq.(10), h_0 accounts for very short term transients during the initial exponential growth period; for a late time, the equation follows the well-known empirical form:

$h(t;,C_0) = \frac{1}{4} C_0 A g t^2$, which exhibits the growth rate: $\alpha = \frac{1}{4} C_0$. Ristorcelli and Clark [47] also

indicated that the asymptotic growth rate (which can be calculated using Eq.9) may not be universal. Moreover, they argue that because the flow depends throughout its lifespan on ICs, the flow cannot ever be regarded as truly self-similar. The acceleration-reversing flows that we consider in this work violate the assumptions of self-similarity of the first kind in more substantive ways, since $g(t)$ appears as an arbitrary time-scale alongside the evolution t., though we consider in later sections the extent to which the re-acceleration phase in isolation can be regarded as self-similar.

In the present work, our benchmark initial perturbation AS(0) matches [12, 17, 22], and we apply an acceleration profile consistent with [22], as depicted in Fig 3. We illustrate typical volume fraction contours of the density field in Fig. 4, with (*i*) vertical slices taken along the center of the domain, and, (*ii*) horizontal slices taken along the interface at corresponding times. Both constant gravity and the ADA profile are shown. The first acceleration reversal leads to a mixed layer that is statically-stable on average and since the Brunt-Vaisalla frequency

($N = \sqrt{\frac{g}{\rho} \frac{\partial \rho}{\partial z}}$) becomes real-valued, we enter a wave-like regime where the mixing layer can

only grow by using residual kinetic energy left over from the accelerating phase to do work against the now stable stratification. We observe that this coincides with a measured reduction of the small-scale anisotropy that characterizes non-linear growth during applied acceleration. It is easily qualitatively identifiable in Fig. 4 that the large coherent structures typical of an

accelerating flow rapidly disintegrates during deceleration, leaving only smaller scales in the flow and a smaller range of densities. This effect is shown by the density contours of the RT mixing layer: *x-z* planar slices taken along the center of the domain (shown in Fig 4-i) and corresponding *x*-y planar slices are taken along *z*=0 (shown in Fig 4-ii). A reduction in the range of densities on a horizontal plane is analogous to increased saturation in a modal decomposition, and [14] thus reducing the subsequent growth rate.

In figure 5, bubble and spike heights are plotted as a function of the length-scale $Z(t)$, defined in Eq.(8). These heights are defined by the *z*- location of the 99% and 1% plane-averaged volume fraction values of the heavy fluid (f_h); the individual heights are measured relative to the original position of the interface ($z = 0$). $<f_h>$ is estimated as follows:

$$< f_h >= \iint f_h dxdy / L^2 \tag{11}$$

and planar averaging <•> of other presented quantities are done in the same manner. The vertical, dashed lines shown in figure 5 (and all subsequent figures) indicate the time instants at which the acceleration was reversed for our ADA problem. At the end of first acceleration period ($Z = 8$), both the bubble and spike heights for the BB case remained at the highest level for bubble height (lowest level for spike height). This was followed by the AS(-2) case whose bubble and spike heights remained between BB and AS(0) cases. The AS(0) case which resulted in the lowest bubble and spike heights. These three cases were all in good agreement with constant acceleration studies of RTI (see Fig 5). Ramaprabhu and Andrews [42] and Banerjee and Andrews [12] reported that the simulations with spectral power in the initial perturbation included at longer wavelengths lead to ($\alpha_{b,s}$) with higher values than narrow-band cases. Broadband cases have larger scales present at *t*=0 and although initially growing more slowly, accumulate considerable inertia and in the long term make a dominant contribution to the

expansion of the mixed layer. The simulations initialized with negative spectral index values (SI=-2), where the perturbation is biased towards longer wavelengths, but whose mode number range was the same as our narrow-band case, exhibited values of ($\alpha_{b,s}$) falling between those of the narrow-band and broadband cases.

Corresponding α_s values for spike heights are shown in Fig. 6 and reveal that during the deceleration period, the growth rate of the mixing layer decays to zero and remains there until the second acceleration phase. This decay rate seems not to be influenced by the details of the initial condition and follows a consistent pattern across all our ADA simulations. We attribute subsequent small oscillations in the growth rate to statistical inhomogeneity in bubble and spike sizes; with a flow in a finite domain in which coherent structures become ever larger and fewer in number, statistical convergence of properties of the horizontal plane will progressively degenerate until averaged quantities begin to reflect the detailed evolution of individual structures. Despite averaged quantities appearing independent of ICs throughout the deceleration phase, we observe that some memory of ICs persists into the second acceleration phase, and layer growth trajectories diverge. This is an observation that we discuss in more detail in coming paragraphs.

As reported by Ramaprabhu et al. [22], after re-acceleration, the flow is RT unstable once more, the rate of molecular mixing decreases and the mixing layer continues its expansion, with familiar and bubble and spike structures re-emerging and interacting to form ever-larger structures. This physical process is illustrated in Fig. 4. We observe in the present work that when comparing the condition of the flow at the point of re-acceleration, although appearing well-mixed, each initial condition has structural differences that depend on prior development and this has a strong influence on the response time of the flow to the impulsive re-introduction

17

of acceleration, Our observations of this behavior in figures 5 and 6 are consistent with Dimonte et al. [23] and we conclude that during deceleration, discernible bubble and spike structures disintegrate and when the buoyancy frequency is real-valued, kinetic and potential energy is transported horizontally around the mixing layer by (energetically conservative) wave-like mechanisms. A delayed return to growth after re-acceleration might be attributed to the time required for small de-correlated perturbations to amplify and mode-coupling to reinstate. In some sense the de-correlation process is equivalent to terminal velocity saturation of existing perturbations so they no longer dominate mode-coupling in the RT-unstable phase. Thus the structure of the flow at the time it enters the deceleration phase has a substantial influence on the later evolution despite apparent convergence of averaged statistics during the re-acceleration.

We found that as the spectral power in the initial perturbation moves towards long wavelengths, the elapsed time is greater between deceleration to acceleration transition and the re-establishment of RT-unstable development. Our narrow-band uniform power case AS(0) was fastest to respond, followed by our narrow-band case with a negative spectral index AS(-2), followed by our broad-band case, as can be seen from values of $\alpha(t)$ in figures 6. As figure 5 shows most clearly, the mixing layer thickness in both the broad-band case and case with negative spectral index follow a rather similar path with trend growth slightly greater than the benchmark of constant acceleration, but after re-acceleration the development of the narrow-band uniform power case is significantly faster than either, and quickly surpasses our benchmark case. To acquire an understanding of this unexpected observation, we were motivated measure parameters that reveal the interior state of the mixing layer.

The horizontally averaged atomic mix parameter θ , defined as:

$$\theta = \frac{\langle f_l f_h \rangle}{\langle f_l \rangle \langle f_h \rangle} \qquad (12)$$

was used to measure the evolution of this quantity at the position of the initial interface, where one would anticipate maximal mixing at a given time. Less-than-complete mixing is a hallmark of rapid growth in the future since horizontal density gradients generate the destabilizing baroclinic torque that perpetuates the RT instability, Another facet of this observation [48, 49], as developed in the next section, is that net mass flux across the plane of the initial interface is a good proxy for growth of the mixing layer; the mass flux is zero in the case of completely mixed $\theta = 1$ fluid, and increases with reducing θ. The value of θ tends [47] to an asymptotic value of $\theta \sim 0.8$ for the constant acceleration case. During the deceleration phase in our recent calculations, the value for θ reaches 1, which corresponds to equal volume fractions of dense and less dense fluid, i.e. completely mixed fluid as resolved at the scale of the computational mesh. Figure 7 presents the evolution of θ with Z, the parameter for mixing layer thickness generalized for variable acceleration. During the first acceleration, the broad-band case produced comparatively low values of θ, implying incomplete mixing and corresponding to future increases in growth rate. This was indeed observed before the onset of deceleration. During the deceleration phase, all cases asymptote towards $\theta \to 1$, reducing the variance of density in the horizontal and, at least in the early stages of re-acceleration, retarding the resumption of unstable growth. Thus it remains difficult to use θ to explain the disparity of trends in future growth, and we probed more detailed statistical quantities to seek understanding of the influence that ICs retain over the long term.

19

3.1.   Second Order Moments

Second order moments provide further detail about the nature of the mixing and the extent to which flows with acceleration reversals can be regarded as self-similar. One requirement for self-similarity is that constant values are required for normalized second order moments at the geometric center-plane, scalar (density) variance *<cc>*, normalized mass flux $<u_3c>/h_{tot}^{0.5}$, and normalized vertical velocity variance $<u_3u_3>/h_{tot}$ [47]. In this study the second order moments were averaged at the center plane (*x-y* plane at *z = 0*) that corresponded to the initial interface location for the calculations. The parameters were normalized by dividing the scalar by the square root of the total mix width ($h_{tot} = h_b + h_s$); the variance was divided by the h_{tot}.

By definition, a low scalar or density variance value corresponds to higher molecular mixing; the limiting case of completely mixed fluid has a scalar variance of zero. During the deceleration phase, where we observed almost completely-mixed fluid within the mixing layer width, all our simulated ICs evolve to a value of zero for the scalar variance as seen in figure 8. As expected, the observed effects for the scalar variance are very similar to those observed for the molecular mix parameter since both parameters are higher-order statistics of the scalar (density) field. The normalized mass flux parameter $<u_3c>/h_{tot}^{0.5}$ is plotted in figure 9. It has been reported in various studies [48, 49] that the mass flux plays a crucial role in the conversion of potential energy to kinetic energy of buoyancy driven flows. During deceleration we have statically-stable flow in a wave-like regime. The natural frequency of the system defined by the Brunt-Vaisalla frequency is real-valued and dependent on the mean gradient of the stratification throughout the mixing layer. Since horizontal transport and exchange of kinetic and potential energy is governed by wave-like behavior, mass flux is bound to oscillate at the same frequency. Indeed in figure 9 a damped oscillation is evident, similar to that reported in [50] where statically

unstable and statically stable mixing layer development was juxtaposed. A zero time-average mass flux indicates that there is no supply of less-well-mixed fluid that could provide potential energy for future growth of the mixing layer. By reaccelerating the system, we regain positive values of the mass flux (see Fig. 9). The increase of mass-flux indicates that less-well-mixed fluids are once again feeding potential energy to the core of the mixing layer and promoting future growth. A corresponding decrease in θ seen in Fig. 7 is consistent with this, and also with the increase of the scalar variance in Fig. 8.

The final second order moment presented is the normalized variance of the vertical component of the velocity field. The mass flux values observed during the deceleration period indicate that there is no net conversion from potential to kinetic energy; the residual kinetic energy in the flow undergoes decay due to viscous dissipation and work is actually being done against the stratification, a net conversion from kinetic to potential energy that is known [51] to sharpen rather than smooth horizontally-averaged vertical density gradients. As illustrated in Fig. 10, a reduction in the value of $<u_3 u_3>/h_{tot}$ was observed during the deceleration phase in all cases, with very little disparity between them.

During deceleration all parameters showed very similar increases in molecular mixing, net mass flux and scalar variance, so by the end of the deceleration phase, on the basis of these metrics there would appear to be little retention of memory of the ICs. This raises several interesting questions; (a) What is the specific mechanism by which sufficient memory is retained to influence subsequent development in the re-acceleration phase? (b) What is the time-scale of recovery to self-similarity of the re-accelerated flow? The impulse response time—which might be defined as: the time between the first instant of re-acceleration until a parameter first touches its asymptotic value—was shortest for our narrow-band case with uniform spectral power, and

longest for our broad-band case, once again consolidating our observation that the distribution of initial spectral power influences development during re-acceleration. We deemed the flow to be approaching self-similarity just before the deceleration phase begins, but the suspension of unstable growth mechanisms, and the introduction of a second time-scale (by specifying the instant of reversal) violates assumptions of self-similarity. However, we are of the opinion that a suitable virtual origin could be found for re-acceleration if one views the prior evolution as simply supplying a requisite initial condition (albeit with non-zero kinetic energy) and self-similarity could be approached eventually. Despite considerable evolution beyond the point of re-acceleration, our simulations did not demonstrate convergence towards self-similarity, though we would argue in principle that in the long term, well beyond the limits of our computational domain, convergence to self-similarity would indeed be recovered.

3.2. Anisotropy Tensors

The anisotropy tensor provides information about the proportion of total kinetic energy associated with a particular direction, and this measure is bounded between -1/3 and +2/3. A value of -1/3 implies no energy in the measured component whereas a value of +2/3 implies all energy is in that component. As a result, B_{33} indicates the amount of total energy in the vertical component while B_{11} and B_{22} refer to the horizontal components and are calculated as:

$$B_{ij} = \frac{<u_i u_j>}{<u_k u_k>} - \frac{1}{3}\delta_i \tag{13}$$

In an isotropic flow, all components of anisotropic tensor are equal, and since $B_{11} = B_{22} = B_{33} = 0$, then from Eq. (13) all components should be zero. A typical RT-unstable flow is horizontally isotropic (where $B_{11}=B_{22}$) and vertically anisotropic. The asymptotic value of B_{33} was reported as ~0.30 by Ristorcelli and Clark [47] which implies ~2/3 of the kinetic energy is associated with

the vertical. The remainder lies in horizontal components of the anisotropy tensor and each of them approaches a value of -0.15. Fig. 11, shows all of the components of the anisotropy tensor for our benchmark constant acceleration case. During the deceleration phase, as the total kinetic energy decayed, the isotropy within the flow increased. Crucially the anisotropy tensor shows substantial dependence on the ICs throughout the deceleration phase, and this is in marked contrast with other measured parameters we have considered. We attribute this behavior to the wave-like mechanisms that govern horizontal transport of energy in the mixing layer during deceleration. Interfacial waves are well-known to follow a dispersion relation of the form: $\omega = f(k, A_t)$, where A_t is the Atwood number, and $k=2\pi/\lambda$ is the mode number. Treating the mixing layer as sharp with respect to an infinite domain, we would expect a range of phase speeds dependent on the spectral distribution present at the acceleration-deceleration transition. Looking more closely at the structure of the mixing layer, the density stratification has a pronounced change in gradient from top to bottom, so the natural frequency of buoyant internal oscillations is not uniform throughout the thickness of the mixing layer. The dispersion relation for such waves is spatially more complex but on average we would expect vertical transmission of energy towards the middle of the mixing layer, focusing energy away from coherent structures at its periphery. We argue that these wave-like and predominantly energy-conserving features will move horizontally with a range of phase speeds, collectively altering the phase relationships between modes and thereby reducing the coherence of individual structures that previously formed bubbles and spikes during initial acceleration. The degree of decorrelation is dependent on the vertical structure of the stratification, and this in turn is particularly dependent on the spatial location of mixing. It becomes clear, viewed from this perspective, why the distribution

of spectral power in the ICs should play such a substantial role in subsequent re-accelerated evolution yet not be observable with mean quantities during deceleration.

Fig. 12 illustrates a marked difference between the broadband case and the other two. With greater power at the long wavelength end of the spectrum, pre-deceleration development of bubbles and spikes will be slower and overall mixing layer growth more strongly dependent on a small number of coherent structures. Should this energy become phase-decorrelated during deceleration, then it is reasonable to believe that re-assembling coherent bubbles and spikes would take comparably longer than in cases where initial acceleration produced more numerous structures that individually were closer to saturation. Indeed Fig. 5 corroborates this view, showing a marked relative increase in growth rate for the shortest wavelength case.

3.3.   Spatial Profiles

Spatial profiles of the second order moments provide information about the structure of the flow. Ristorcelli and Clark [47] report spatial profiles of second order moments for their RTI simulations under constant acceleration. Since their simulations were well within the Boussinesq regime at A_t=0.01, it results in strongly symmetric material transport on both sides of the geometric centerline. However, our study focusses on cases outside the Boussinesq regime (moderate $A_t = 0.5$) and non-Boussinesq effects are observed to significantly affect the spatial distribution of material, and symmetry about the interface is lost.

We start the discussion by reporting spatial profiles of parameters for our constant acceleration and ADA profiles for our benchmark initial condition [AS(0)]; the objective is to understand the changes that the acceleration history makes to spatial evolution without complexity introduced by modifying initial spectra (see Figs. 13, 14 and 15).

The horizontal axis of these figures, which display the spatial extents, correspond to the non-dimensional vertical height of the domain. In Figs. 13-15, where the time evolution of the spatial moments are presented, the non-dimensionalizing is made by the half of the total mix width $h_{tot}/2$ for the base case AG(0)-CG from the Z value of 32 for all cases. This allows us to analyze how the moments are filling the domain. In Figs 16 -19, again the total mix width $h_{tot}/2$ of the base case AG(0)-CG from the corresponding Z values were used. Note that, in figures 13-15, the values of moments are from the different Z values; thus they did not fill the similar amount of the domain so they do not match; however, in figures 16-19 the values of moments are from the same Z value for all cases. The top and bottom boundary conditions were zero-flux, therefore vertical velocity and scalar variance values were zero at these extremes of the domain (see Fig.s 13 and 15). Likewise, the vertical component of the anisotropy tensors was B_{33}=-0.33, indicating (see Fig. 14) no energy in that component. For Boussinesq case spatial profiles of the second order, moments correspond fairly well with a Gaussian distribution [47], whereas non-Boussinesq effects led to a central plateau as seen in Fig. 13. This plateau might be called the "mixing core", which in our simulations lies between mean material volume fractions of roughly 40% and 60%. We can also identify an edge region, beyond roughly 5% and 95% volume fractions [47], and a transition region from volume fractions 5% to 40%, and 60% to 95%, velocity variance data also indicates the existence of a mixing core (see Fig.13).

Although the central plateau is the most obvious indicator of non-Boussinesq behavior, as seen in Figure 5, heavier fluid penetrates into lighter fluid faster than light penetrates into heavy. This disparity is evident in Figs. 13-15, as the edge region of mixing layer occurs at differing distances from the interface on either side. as shown most clearly by the red line in Fig. 15 which starts from non-dimensional z-value of *-1.2* but ends at a value of *1*. The asymmetry in Fig. 15

might be also attributed to light fluid mixing more rapidly than heavier fluid, similar to the observation reported by Livescu and Ristorcelli [52] . Since the molecular mixing increases during the deceleration period, the asymmetry becomes more pronounced by the end of deceleration period. Examining the anisotropy tensor in Fig. 14, we see that except at the edges of the domain, the velocity field is anisotropic even well within the region of pure unmixed fluids. Here, the vertical component of the velocity anisotropy tensor is around 0.1. In contrast to the velocity and scalar variance, the anisotropy tensor spatial profile is similar to a step function centered on the edge of the mixing layer and suddenly increases to values around 0.3, the asymptotic value of B_{33} that we observe within an RT mixing layer.

Spatial profiles are also presented in figures 16-19 since these metrics clearly delineate differences between ICs. We note that statistical properties of the edge regions are most sensitive to changes in ICs, but the transition regions are rather less so in all cases. At the end of first acceleration period ($Z=8cm$), our case with broadband uniform spectral power had the greatest vertical extent of non-zero velocity variance, consistent with having the most rapid mixing layer growth. In keeping with our earlier observations (see Fig. 5), the long-wavelength biased narrow-band case follows with next most extended region of non-zero velocity variance, followed by the case with narrowband uniform spectral power (see Fig. 17). As mentioned earlier, the deceleration phase appears to reduce the sensitivity of second order moments to ICs and their spatial profiles support this observation. Throughout deceleration (until $Z=16cm$), velocity and scalar variances tend to zero as the flow during this phase of evolution is statically stable so there is no new supply of potential energy and instead reserves of existing kinetic energy are being drawn down in doing work against the stratification.

Scalar variance inevitably reduces with the degree of mixedness, and in figure 19 we see asymmetry in the scalar variance that we attribute to the fluid of smaller density having a greater propensity to mix, as remarked above. On the other hand, the anisotropy tensor (see Fig. 18) exhibited continual fluctuations with considerable amplitude even once deceleration has ceased, although there emerges no clear trend as a function of the spectral distribution of ICs. Upon re-acceleration, spatial profiles of velocity and scalar variance showed some dependency on initial spectra. Meanwhile, the vertical component of the anisotropy tensor fluctuates around its asymptotic value of 0.3, showing little discernable variation between sets of ICs.

4. CONCLUSION

The problem of variable-acceleration RTI was investigated to understand how variation in the distribution of spectral power in the ICs influences late-time evolution. Simulations were performed using a massively parallel three–dimensional, variable-density, incompressible flow solver, MOBILE. The acceleration history, an ADA sequence, was common to all cases simulated, except for a benchmark constant acceleration case that was used to compare against the large body of existing literature on mixing in RT unstable flows. Three distinct ICs were selected, one with uniform spectral power over a broad range of wavelengths, one with a narrower bandwidth but the same total spectral power, and one with a biased distribution of power towards longer wavelengths that in some sense forms an intermediate case between the two.

During the first acceleration phase, results were consistent with existing literature [12, 13, 19] and confirmed that cases initialized with spectral power towards longer wavelengths grow fastest. During deceleration the flow is statically stable in density, there is no resource of potential energy to fuel further growth of the mixing layer and instead work is done against the

27

stable stratification using residual kinetic energy provided from the earlier acceleration phase. The anisotropy associated with rapid RT-unstable growth becomes insignificant; the mixing layer becomes increasingly well-mixed. With a real-valued buoyancy frequency, energy is transported horizontally within the mixing layer by internal- and interfacial-wave-like processes. Following the dispersion relation for such waves, their evolution leads to de-correlation of the previously coherent bubble and spike structures, and the manner in which this occurs has a significant influence on growth rates in the following re-acceleration. Flow during re-acceleration is thus sensitive to spectral power in ICs, despite there being an apparent reduction in sensitivity to lower order statistics throughout the deceleration phase. Some higher order statistics are sensitive during deceleration, in particular those that measure, however indirectly, the phase relationships between modes. In the long-term the re-accelerated flow is consistent with an asymptotic convergence towards self-similarity; the first acceleration and subsequent deceleration can be viewed simply as a providing an initial condition with non-zero kinetic energy.

ACKNOWLEDGEMENT

REFERENCES

1. Rayleigh, L., *Investigation of the equilibrium of an incompressible heavy fluid of variable density.* Proceedings of Royal Society of London, 1884. **14**: p. 170-177.
2. Taylor, G.I., *The instability of liquid surfaces when accelerated in a direction perpendicular to their planes I.* . Proceedings of Royal Society of London Series A, 1950. **201**: p. 192-196.
3. Veynante, D., et al., *Gradient and counter-gradient scalar transport in turbulent premixed flames.* Journal of Fluid Mechanics, 1997 **332**: p. 263-293.
4. Veynante, D. and L. Vervisch, *Turbulent combustion modeling.* Progress in Energy Combustion Science, 2002. **28**: p. 193-266.
5. Britter, R.E. and S.R. Hanna, *Flow and dispersion in urban areas.* Annual Review of Fluid Mechanics, 2003. **35**: p. 469-496.
6. Adkins, J.F., K. McIntyre, and D.P. Schrag, *The salinity, temperature, and $\delta^{18}O$ of the glacial deep ocean.* Science, 2002. **298**: p. 1769-1773.
7. Wunsch, C. and F. R., *Vertical mixing, energy, and the general circulation of oceans.* Annual Review of Fluid Mechanics, 2004. **36**: p. 281-314.
8. Lindl, J.D., *Inertial confinement fusion: the quest for ignition and energy gain using indirect drive*. 1998, Berlin: Springer.
9. Nakai, S. and H. Takabe, *Principles of inertial confinement fusion-physics of implosion and the concept of inertial fusion energy.* Report of Progress in Physics, 1996. **59**: p. 1071-1131.
10. Gull, S.F., *The X-ray, optical and radio properties of young supernova remnants.* Royal Astronomical Society Monthly Notices, 1975. **171**: p. 263-278.
11. Colgate, S.A. and R.H. White, *The hydrodynamic behavior of supernova explosions.* Astrophysical Journal, 1966. **143**: p. 626-681.
12. Banerjee, A. and M.J. Andrews, *3-D Simulations to investigate initial condition effects on the growth of Rayleigh-Taylor mixing.* International Journal of Heat and Mass Transfer, 2009. **52**: p. 3906-3927.
13. Livescu, D., T. Wei, and M.R. Petersen, *Direct Numerical Simulations of Rayleigh-Taylor instability.* Journal of Physics: Conference Series, 2011. **318**(8): p. 082007.
14. Linden, P.F., J.M. Redondo, and D.L. Youngs, *Molecular mixing in Rayleigh Taylor instability.* Journal of Fluid Mechanics, 1994. **265**: p. 97-124.
15. Anuchina, N.N., et al., *Turbulent mixing at an accelerating interface between liquids of different densities.* Fluid Dynamics, 1978. **13**(6): p. 916-920.
16. Youngs, D.L., *Numerical simulation of turbulent mixing by Rayleigh-Taylor instability.* Physica D, 1984. **12**: p. 32-44.
17. Dimonte, G., et al., *A comparative study of the turbulent Rayleigh-Taylor (RT) instability using high-resolution 3D numerical simulations: The Alpha-Group collaboration,.* Physics of Fluids, 2004. **16**: p. 1668-1693.
18. Ramaprabhu, P. and M.J. Andrews, *On the initialization of Rayleigh-Taylor simulations.* Physics of Fluids, 2004. **16**: p. L59-L62.
19. Ramaprabhu, P., G. Dimonte, and M.J. Andrews, *A numerical study of the influence of initial perturbations on the turbulent Rayleigh-Taylor instability.* Journal of Fluid Mechanics, 2005. **536**: p. 285-319.

20. Dimonte, G. and M. Schneider, *Turbulent Rayleigh-Taylor instability experiments with variable acceleration.* Physical Review E, 1996. **54**: p. 3740-3743.

21. Livescu, D. and T. Wei, *Direct Numerical Simulations of Rayleigh-Taylor instability with gravity reversal.* Seventh International Computationl Fluid Dynamics (ICCFD7), 2012: p. 9-13.

22. Ramaprabhu, P., V. Karkhanis, and A.G.W. Lawrie, *The Rayleigh-Taylor Instability driven by an accel-decel-accel profile.* Physics of Fluids (1994-present), 2013. **25**(11): p. 115104.

23. Dimonte, G., P. Ramaprabhu, and M.J. Andrews, *Rayleigh-Taylor instability with complex acceleration history.* Physical Review E, 2007. **76**: p. 046313.

24. Lawrie, A.G.W., *On Rayleigh-Taylor mixing: confinement by stratification and geometry.* 2009, University of Cambridge.

25. Lawrie, A.G.W. and S.B. Dalziel, *Turbulent diffusion in tall tubes. I. Models for Rayleigh-Taylor instability.* Physics of Fluids (1994-present), 2011. **23**(8): p. -.

26. Lawrie, A.G.W. and S.B. Dalziel, *Turbulent diffusion in tall tubes. II. Confinement by stratification.* Physics of Fluids (1994-present), 2011. **23**(8): p. -.

27. Helmholtz, H., *Über Integrale der hydrodynamischen Gleichungen, welcher der Wirbelbewegungen entsprechen (On integrals of the hydrodynamic equations which correspond to vortex motions).* Journal für die reine und angewandte Mathematik, 1858. **55**: p. 25-55.

28. Strang, G., *On the Construction and Comparison of Difference Schemes.* SIAM Journal on Numerical Analysis, 1968. **5**(3): p. 506-517.

29. Ramaprabhu, P. and M.J. Andrews, *Experimental investigation of Rayleigh–Taylor mixing at small Atwood numbers.* Journal of Fluid Mechanics, 2004. **502**: p. 233-271.

30. Mueschke, N.J., M.J. Andrews, and O. Schilling, *Experimental characterization of initial conditions and spatio-temporal evolution of a small-Atwood-number Rayleigh–Taylor mixing layer.* Journal of Fluid Mechanics, 2006. **567**: p. 27-63.

31. Cabot, W.H. and A.W. Cook, *Reynolds number effects on Rayleigh-Taylor instability with possible implications for type-Ia supernovae.* Nature Physics, 2006. **2**: p. 562-568.

32. Young, Y.N., et al., *On the miscible Rayleigh-Taylor instability: two and three dimensions.* Journal of Fluid Mechanics, 2001. **447**: p. 377-408.

33. Llor, A., *Bulk turbulent transport and structure in Rayleigh–Taylor, Richtmyer–Meshkov, and variable acceleration instabilities.* Laser and Particle Beams, 2003. **21**(03): p. 305-310.

34. Poujade, O. and M. Peybernes, *Growth rate of Rayleigh-Taylor turbulent mixing layers with the foliation approach.* Phys Rev E Stat Nonlin Soft Matter Phys, 2010. **81**(1 Pt 2): p. 26.

35. Gréa, B.-J., *The rapid acceleration model and the growth rate of a turbulent mixing zone induced by Rayleigh-Taylor instability.* Physics of Fluids (1994-present), 2013. **25**(1): p. 015118.

36. Mikaelian, K.O., *Analytic approach to nonlinear hydrodynamic instabilities driven by time-dependent accelerations.* Physical Review E, 2010. **81**(1): p. 016325.

37. Peltier, W.R. and C.P. Caulfield, *Mixing Efficiency in Stratified Shear Flows.* Annual Review of Fluid Mechanics, 2003. **35**(1): p. 135-167.

38. Dimonte, G., *Dependence of turbulent Rayleigh-Taylor instability on initial perturbations.* Physical Review E, 2004. **69**(5): p. 056305.

39. Mueschke, N.J., M.J. Andrews, and O. Schilling, *Experimental characterization of initial conditions and spatio-temporal evolution of a small Atwood Rayleigh-Taylor mixing layer.* Journal of Fluid Mechanics, 2006. **567**: p. 27-63.

40. Mueschke, N.J. and O. Schilling, *Investigation of Rayleigh–Taylor turbulence and mixing using direct numerical simulation with experimentally measured initial conditions. I. Comparison to experimental data.* Physics of Fluids, 2009. **21**: p. 014106.

41. Banerjee, A. and L. Mutnuri, *Passive and Reactive Scalar Measurements in a Transient High Schmidt-number Rayleigh-Taylor Mixing Layer* Experiments in Fluids, 2012. **53**: p. 717-729.

42. Ramaprabhu, P. and M.J. Andrews, *Experimental investigation of Rayleigh- Taylor mixing at small Atwood numbers.* Journal of Fluid Mechanics, 2004. **502**: p. 233-271.

43. Haan, S.W., *Onset of nonlinear saturation for Rayleigh-Taylor growth in the presence of a full spectrum of modes.* Physical Review A, 1989. **39**(11): p. 5812-5825.

44. Wei, T. and D. Livescu, *Late-time quadratic growth in single-mode Rayleigh-Taylor instability.* Physical Review E, 2012. **86**(4): p. 046405.

45. Andrews, M.J., *Accurate Computation of Convective Transport in Transient Two-Phase Flow.* International Journal for Numerical Methods in Fluids 1995. **21**(3): p. 205-222.

46. Dimonte, G. and M. Schneider, *Density ratio dependence of Rayleigh-Taylor mixing for sustained and impulsive acceleration histories.* Physics of Fluids, 2000. **12**: p. 304-321.

47. Ristorcelli, J.R. and T.T. Clark, *Rayleigh-Taylor turbulence: self-similar analysis and direct numerical simulations. .* Journal of Fluid Mechanics, 2004. **507**: p. 213-253.

48. Livescu, D. and J.R. Ristorcelli, *Buoyancy-driven variable density turbulence.* Journal of Fluid Mechanics, 2007. **591**: p. 43-71.

49. Cook, A.W., W. Cabot, and P.L. Miller, *The mixing-transition in Rayleigh-Taylor instability.* Journal of Fluid Mechanics, 2004. **511**: p. 333-362.

50. Lawrie, A.G.W. and S.B. Dalziel, *Rayleigh–Taylor mixing in an otherwise stable stratification.* Journal of Fluid Mechanics, 2011. **688**: p. 507-527.

51. Fernando, H.J.S., *Turbulent Mixing in Stratified Fluids.* Annual Review of Fluid Mechanics, 1991. **23**: p. 455-493.

52. Livescu, D. and J.R. Ristorcelli, *Variable-density mixing in buoyancy-driven turbulence.* Journal of Fluid Mechanics, 2008. **605**: p. 145-180.

Table 1. List of simulations reported in the current work

| Shorthand Reference	Wave-number range	Spectral index	Acceleration History
AS(0)-CG	32-64	0	Constant Gravity
AS(0)	32-64	0	A-D-A
AS(-2)	32-64	-2	A-D-A
BB	4-64	0	A-D-A
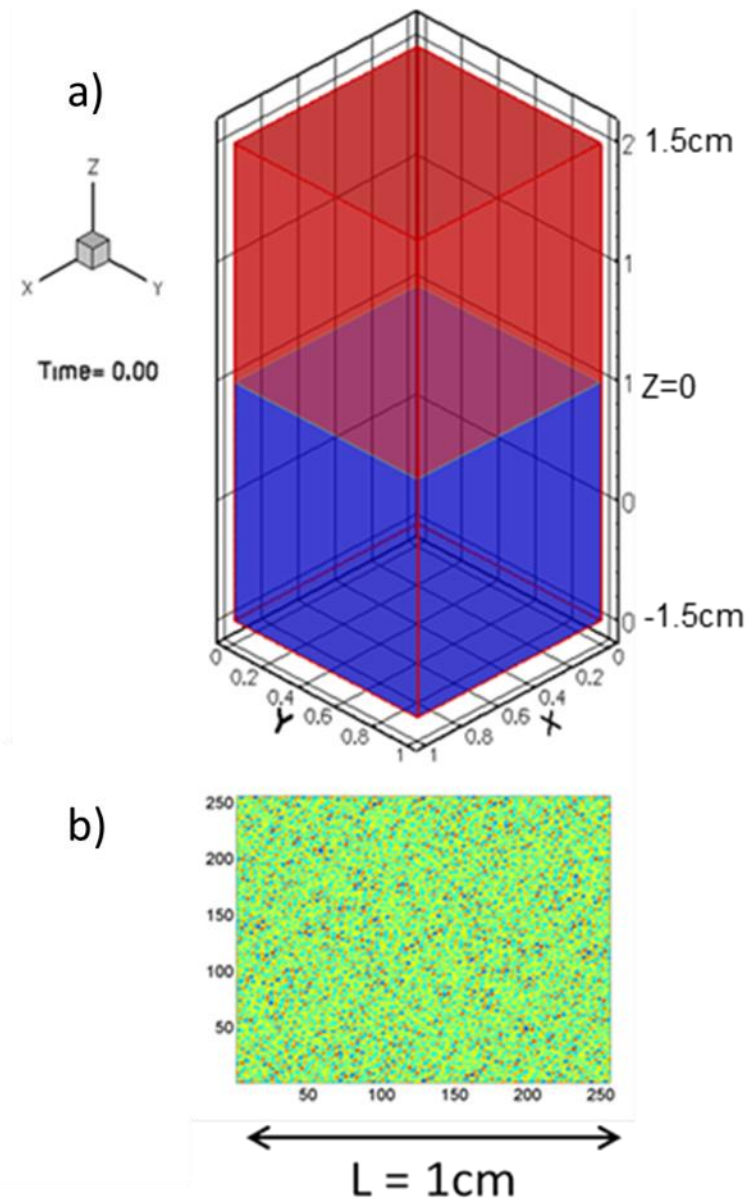
Figure 1. (a) Schematic of the computational domain used in simulations. The box size is $1 \times 1 \times 3$ cm (in the x-, y- and z- directions) with densities $\rho_1 = 3.0$ g/cm^3 (red: heavy), $\rho_2 = 1.0$ g/cm^3 (blue: light). (b) Contour plot of initial amplitudes at center-plane ($z = 0$); the amplitudes correspond to annular narrowband ICs with energy in modes 32-64
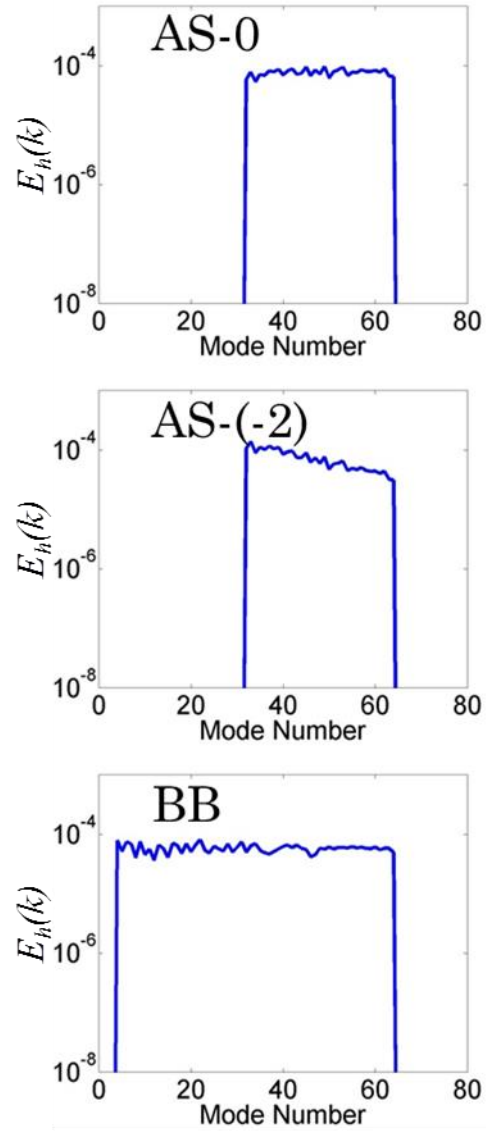
Figure 2. Azimuthally averaged ICs for all simulation cases listed in Table 1 with a root mean square amplitude of 3.15×10^{-4} *L* (where domain size is *L×L×L*)
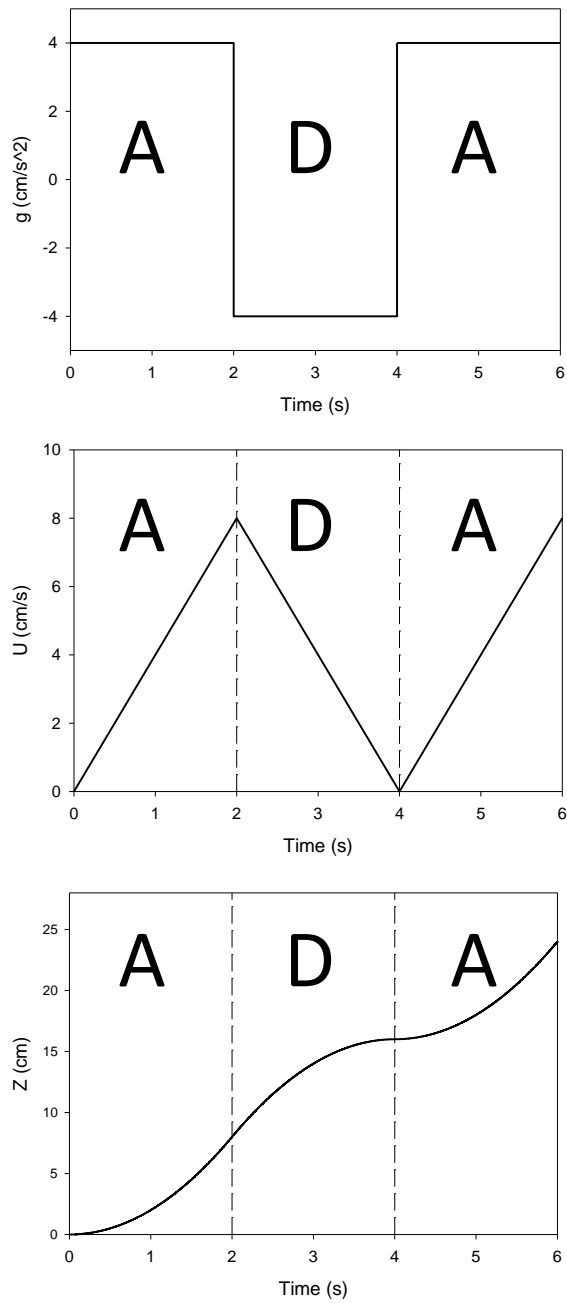
Figure 3. Profiles of (a) acceleration, (b) velocity, and, (c) Z(t) length-scale for the accel-decel-accel (A-D-A) acceleration history.
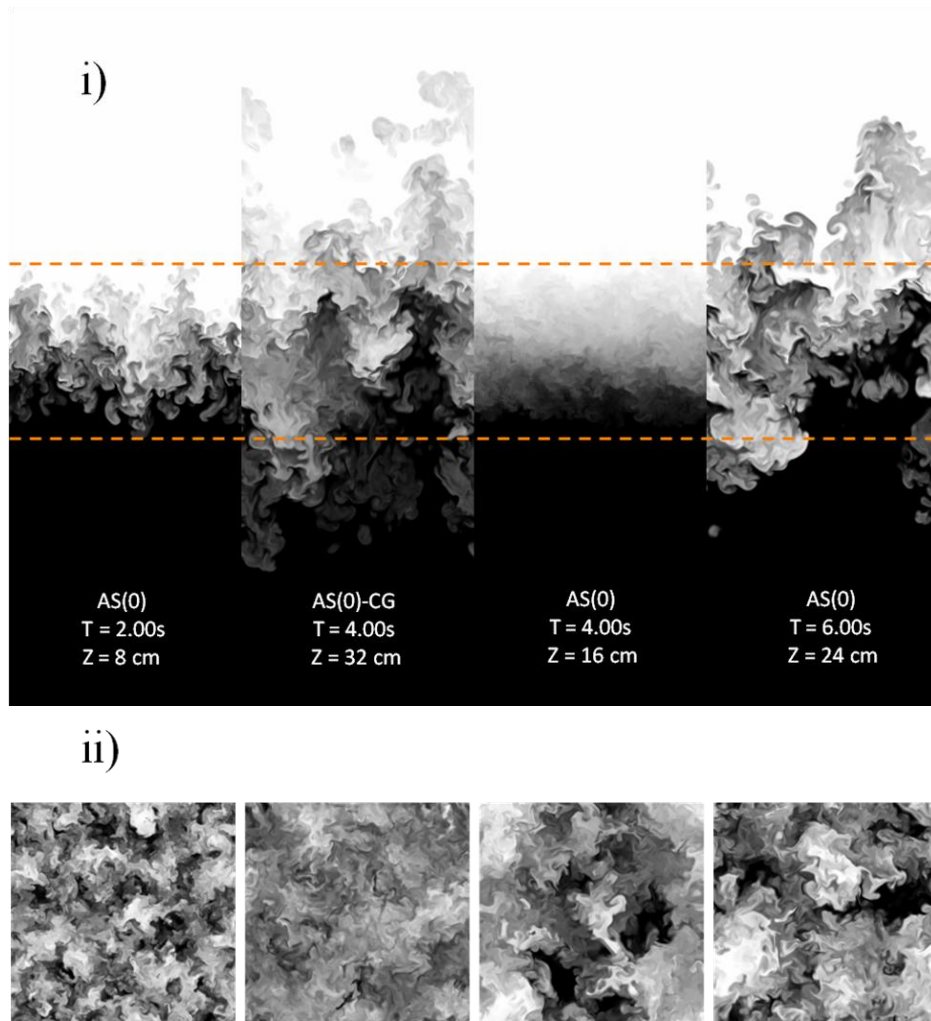
Figure 4. Density contours of the RT mixing layer (i) *x-z* planar slices taken along the center of the domain; cases are defined in table 1. The vertical red dashed lines indicating the edge of the mixing layer width of AS(0)-CG and AS(0) ADA cases. (ii) corresponding *x-y* planar slices are taken along *z=0*.
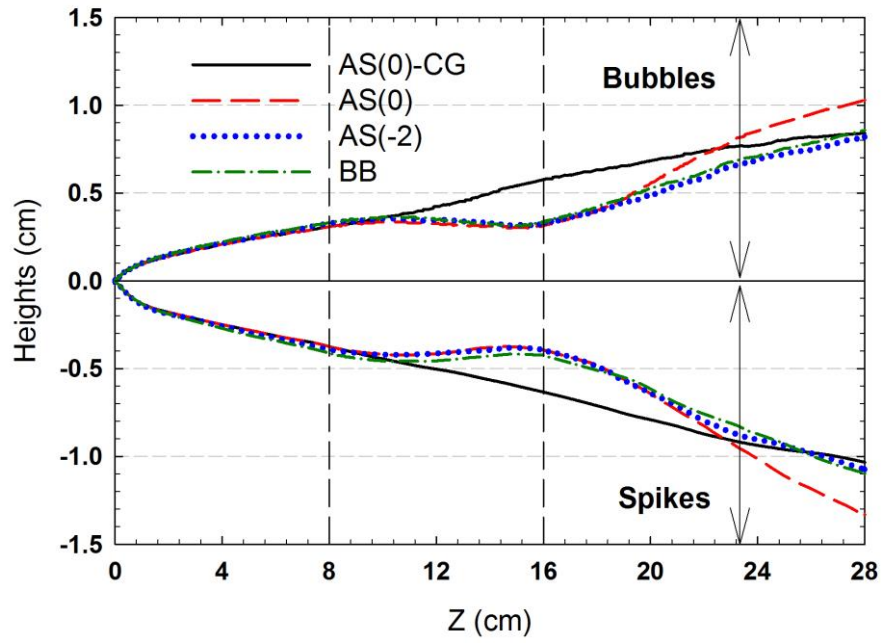
Figure 5. Evolution of the bubble (h_b) and spike heights (h_s) versus interface displacement (Z). Linear growth through the origin would represent quadratic growth from zero amplitude.
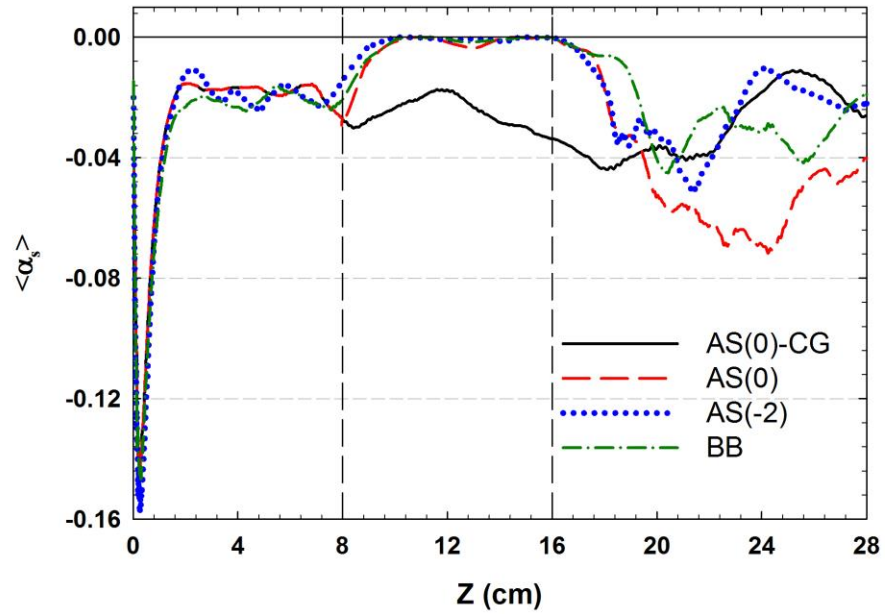
Figure 6. Evolution of the growth constant (α_s) for spikes versus interface displacement (Z).
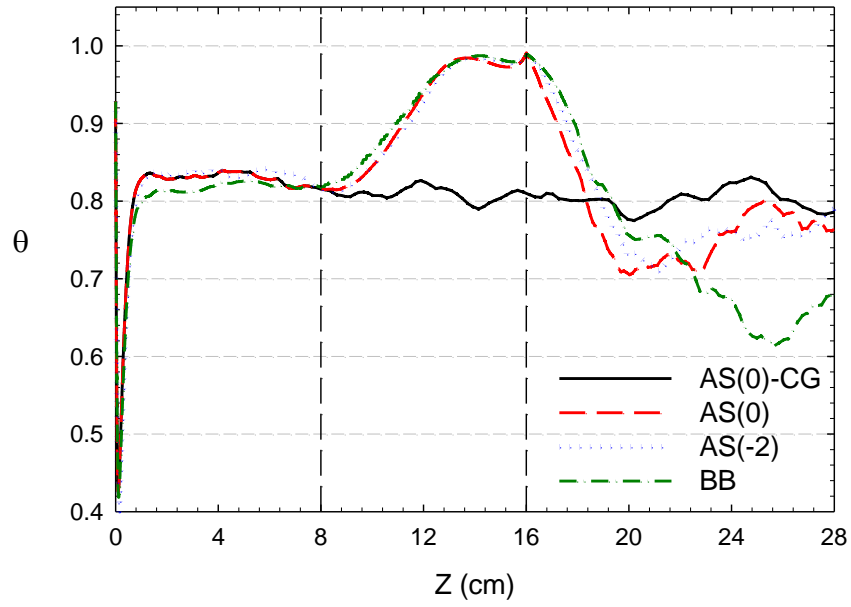
Figure 7. Evolution of the global mix parameter (θ) versus interface displacement (Z).
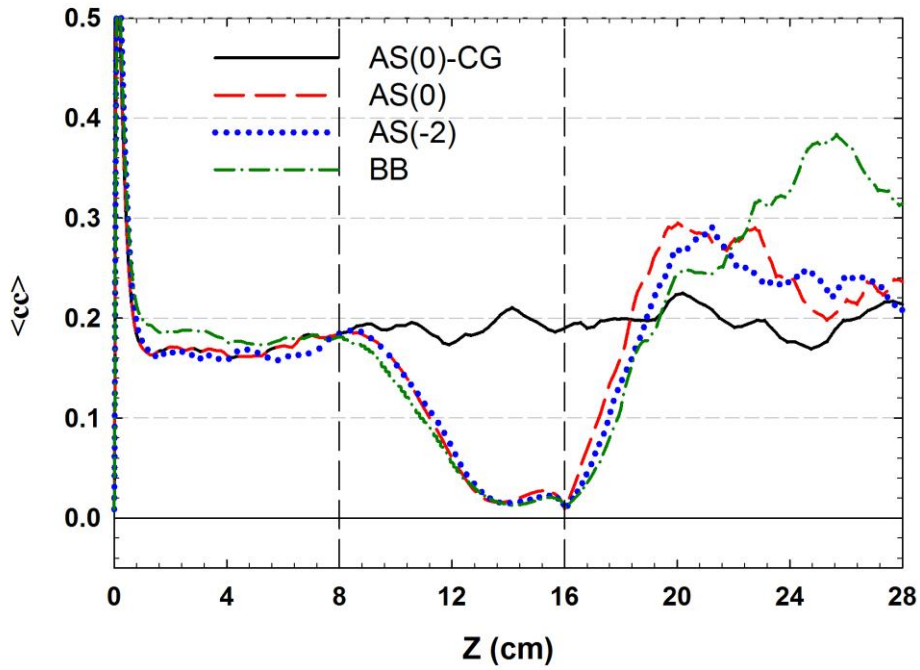
Figure 8. Evolution of scalar variance ($<cc>$) versus interface displacement (Z).
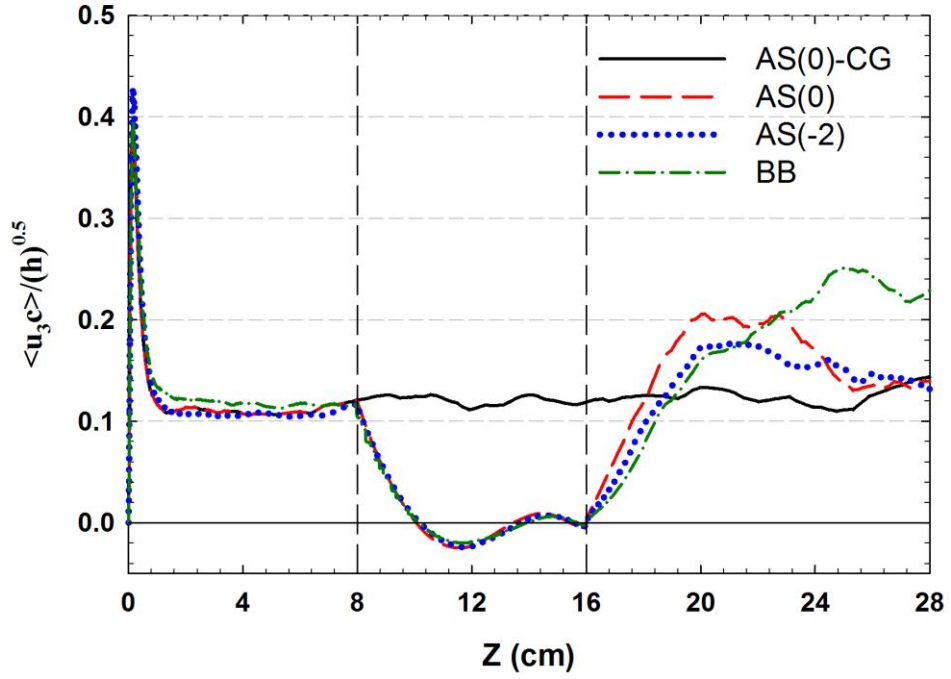
Figure 9. Evolution of normalized mass flux ($<u_3c>/h_{tot}^{0.5}$) versus interface displacement (Z).
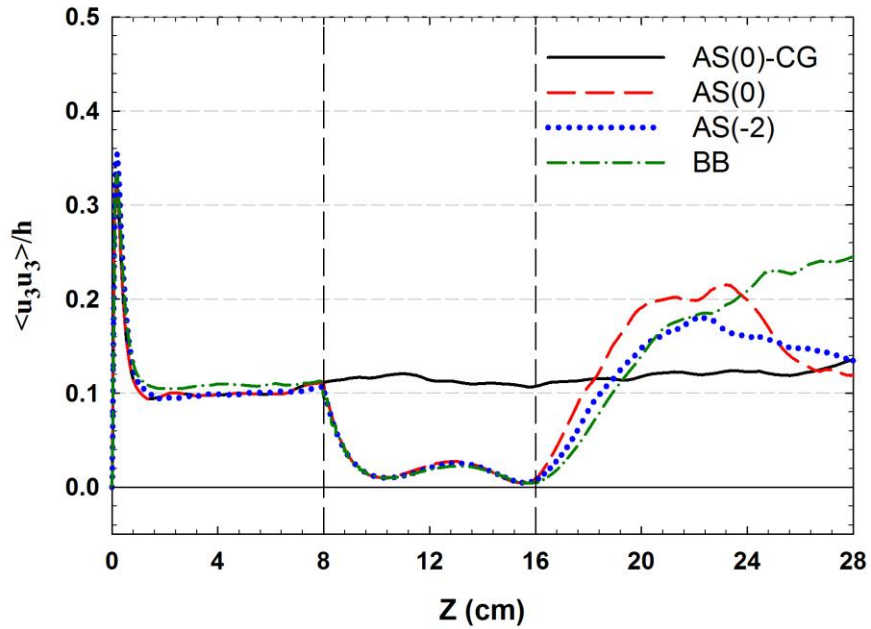
Figure 10. Evolution of normalized vertical velocity variance ($<u_3u_3>/h_{tot}$) versus interface displacement (Z).
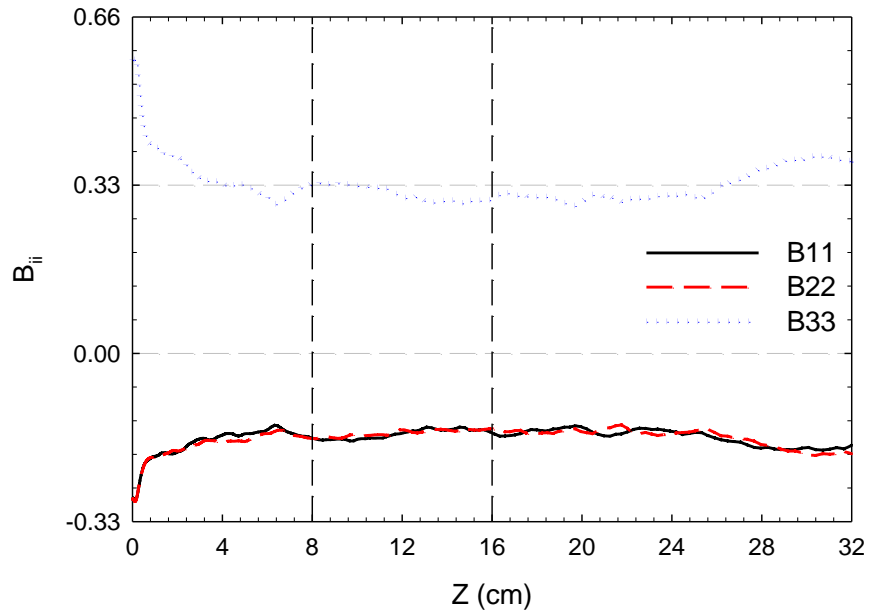
Figure 11. Evolution of Anisotropy Tensors B_{33}, B_{11} and B_{22} for constant acceleration case versus interface displacement (Z).
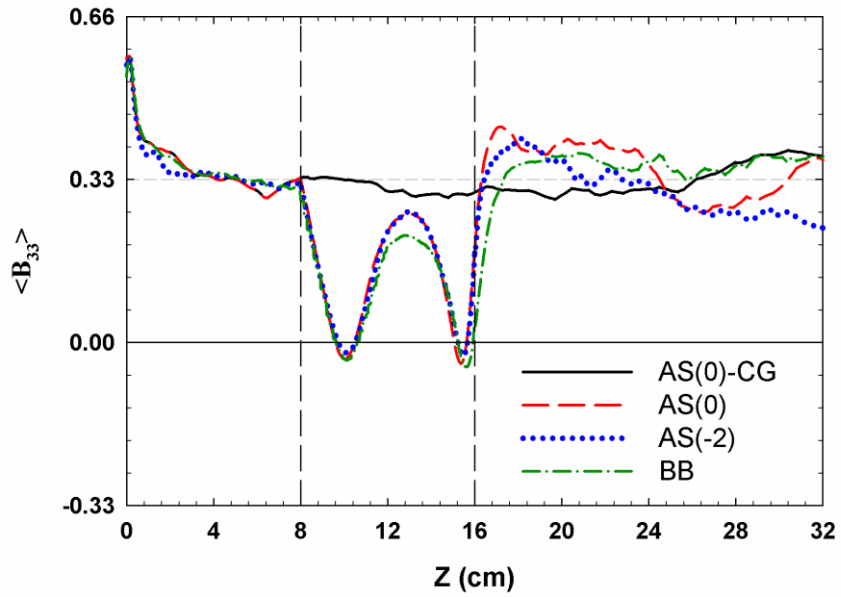
Figure 12. Evolution of Anisotropy Tensor B_{33} versus interface displacement (Z).
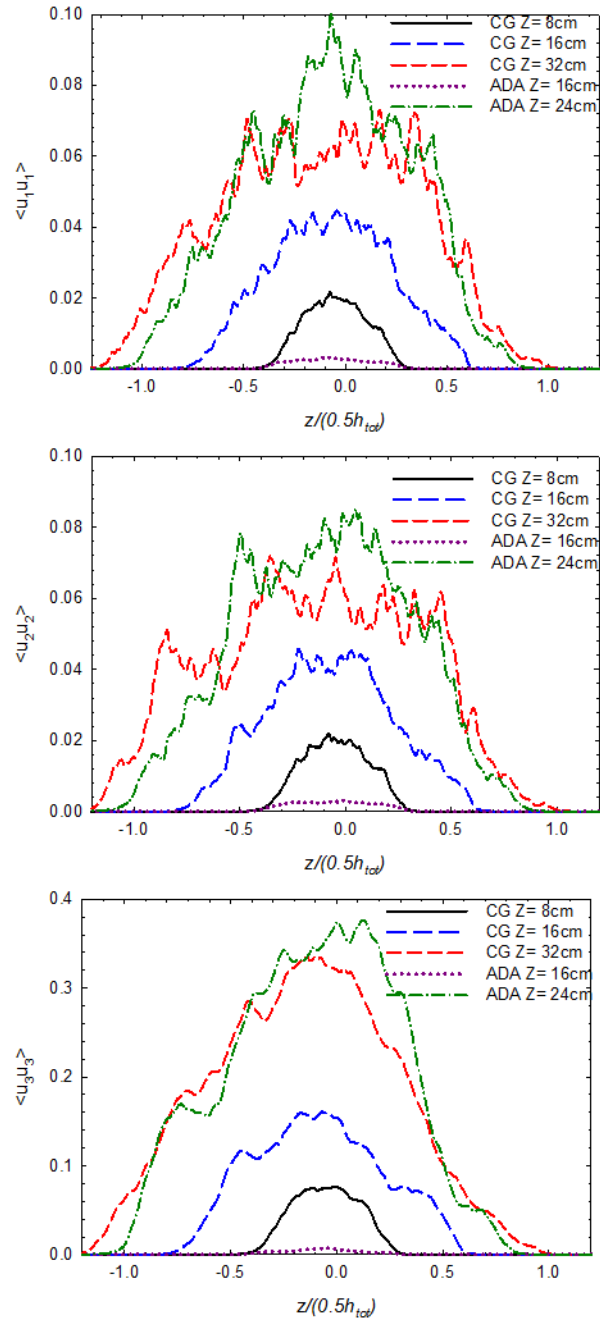
Figure 13. Spatial profiles of a) $\langle u_1 u_1 \rangle$, b) $\langle u_2 u_2 \rangle$ and c) $\langle u_3 u_3 \rangle$ for both CG_AS-0 and AS-0 at different Z values.
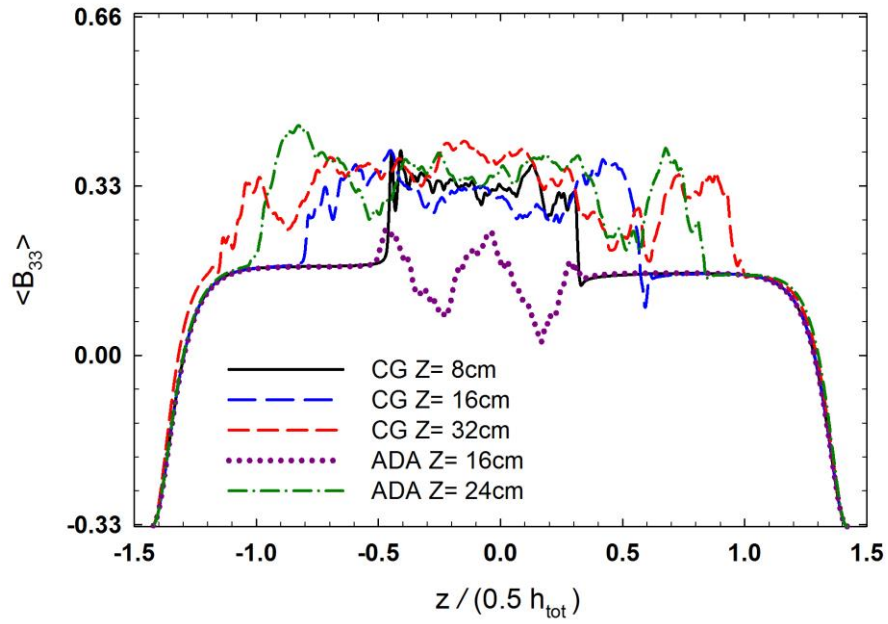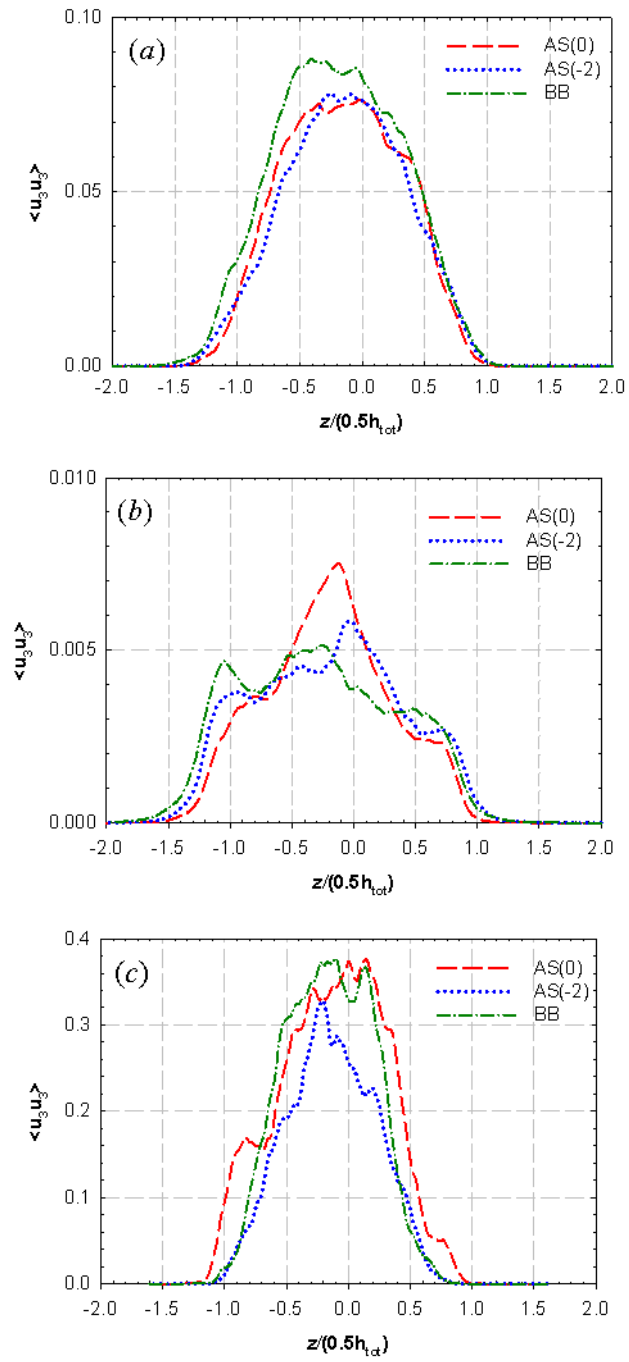
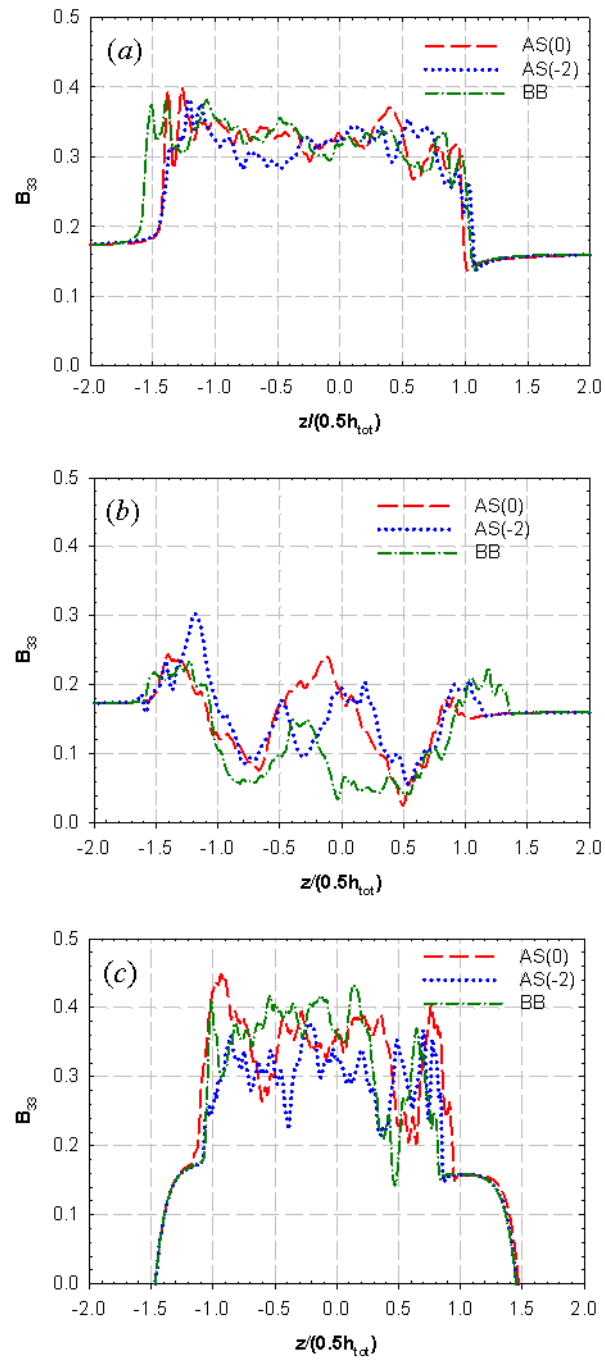**Figure 14.** Spatial profiles of B_{33} for both CG_AS-0 and AS-0 at different Z values.
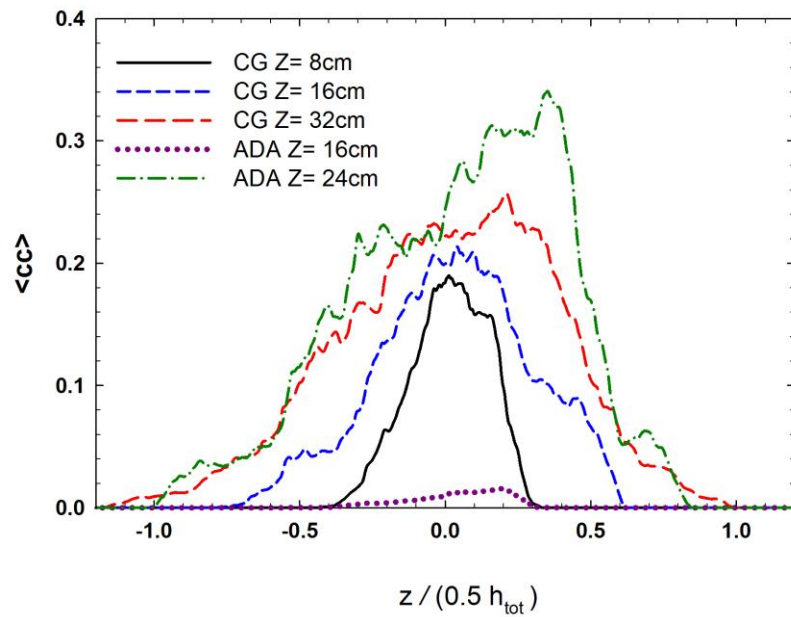
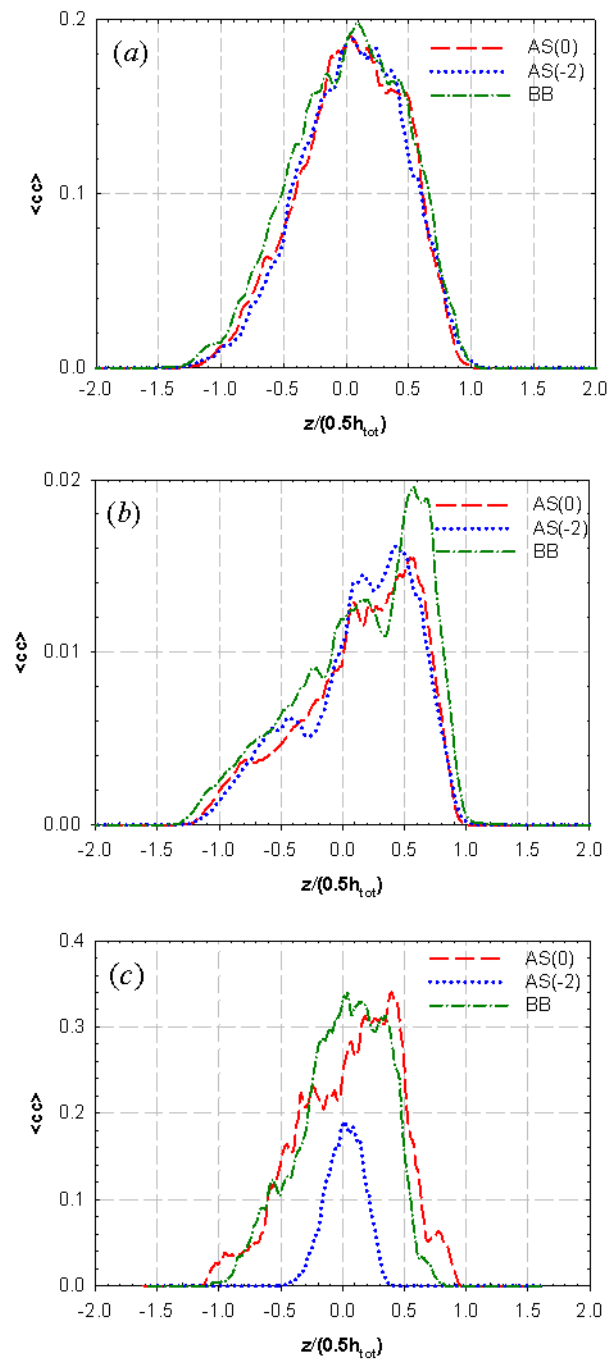**Figure 15.** Spatial profiles of $<cc>$ for both CG_AS-0 and AS-0 at different Z values.
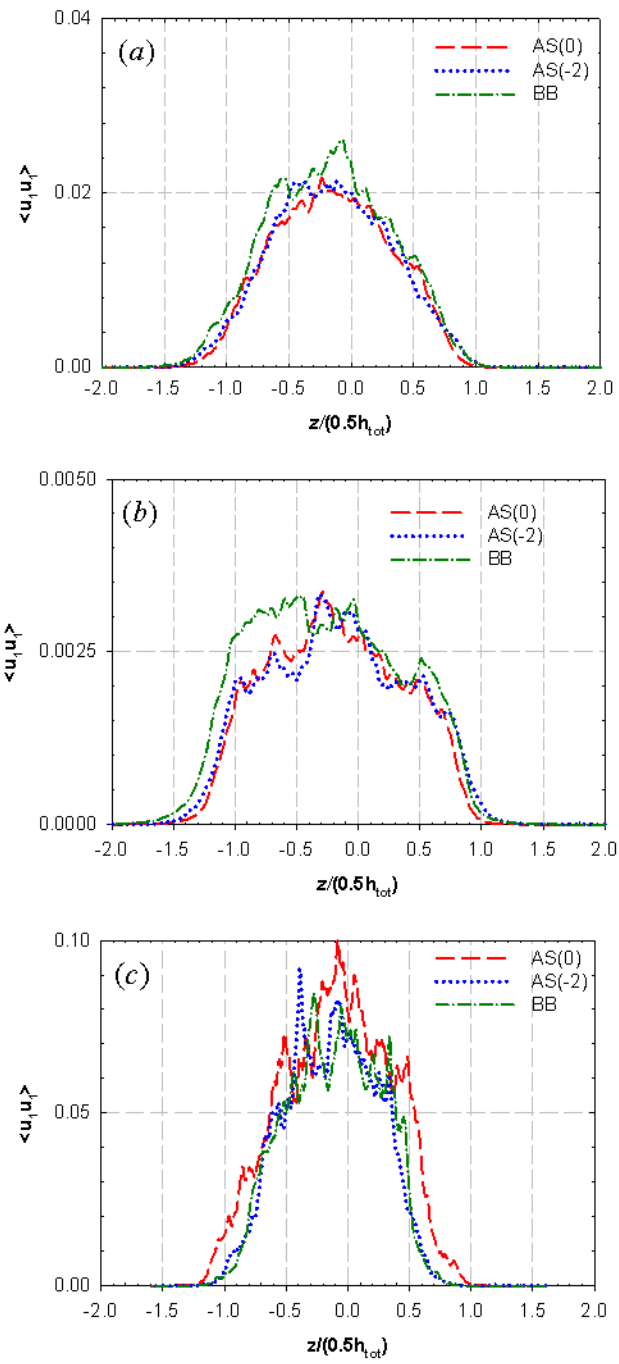
Figure 16. Spatial profiles of $\langle u_1 u_1 \rangle$ at a) Z= 8 cm b) Z =16 cm and c) Z=24 cm for all ICs.

Figure 17. Spatial profiles of $\langle u_3 u_3 \rangle$ at a) Z= 8 cm b) Z =16 cm and c) Z=24 cm for all ICs.

Figure 18. Spatial profiles of B_{33} at a) Z= 8 cm b) Z =16 cm and c) Z=24 cm for all ICs.

Figure 19. Spatial profiles of <cc> at a) Z= 8 cm b) Z =16 cm and c) Z=24 cm for all ICs.